J. Phys. Res. Edu., Vol. 2, March 2025

Exploring AC Conductivity and Microstructure of Iron-Vanadium Doped Systems

Jiban Ghosh and Sanjib Bhattacharya*

Composite Materials Research Laboratory, UGC-HRDC (Physics),

University of North Bengal, District: Darjeeling-734013, West Bengal India.

The present work focuses on the impact of partial substitution of ZnO (former) by various other oxides in the microstructure and AC conductivity of newly developed amorphous semiconducting systems containing two transition metal ions such as vanadium and iron. The current materials may be significantly helpful in specialized applications like high-power lasers for their high refractive indices. An insightful study of the composition-dependent microstructure and electrical transport behavior with various former-modifier ratios is of great interest, not only from an application perspective but also for academic purposes.

I. INTRODUCTION

In recent times, glassy systems have emerged as significant materials for their extensive applications, compositional versatility, and adaptable properties [1, 2]. The transition metal oxides (TMOs) doped glassy system has garnered attention because of its excellent semiconducting nature [3–5]. This characteristic is crucial for numerous devices, including cathode materials in batteries, thermal and mechanical sensors, and electrical and optical memory switching [6]. Electrical conduction processes in glassy systems containing vanadium pentoxide have been studied more extensively than those in other TMOs, as they play a significant role in various solid-state devices [1]. Microscopic investigations suggest that larger crystallites develop at high vanadium concentrations, while a denser distribution of smaller crystallites occurs at lower concentrations of the vanadium compound [7]. Mott's work [1] has successfully explained the mechanism of polaron hopping in terms of phonon-aided electron hopping between V^{4+} and V^{5+} states in the vanadate glassy system. Several microscopic studies indicate that smaller crystallites are formed when the amount of vanadium compound is low, whereas larger crystallites form when the concentration is high [8–11]. Rao et al. [12] described the amorphous nature of the Bi_2O_3–PbO–V_2O_5 glassy system based on their investigations of its direct current (DC) conductivity and structural characterization. Research on glassy systems prepared by substituting various metal oxides for PbO in PbO–V_2O_5 system has revealed that, with dopants like ZnO and TeO_2, n-type conduction can be converted to p-type conduction at higher temperatures [13]. Moreover, in the temperature range of 300–500 K, conduction can be significantly enhanced with dopants such as Bi_2O_3, GeO_2, and TeO_2 [9–13]. Hasegawa et al. [14] established the nature of electrical conductiv-

ity of polycrystalline TeO_2 below 400 °C with respect to temperature. The relationship between electrical conductivity and oxygen partial pressure at a given temperature has also been established, which indicates the role of TeO_2 in the amorphous semiconducting system in the low-temperature region [14]. Jain and Garg [15] interpreted the facts and figures of current-voltage behavior of TeO_2 thin films using Al electrodes. The primary objectives of the present work can be summarized as follows: Firstly, to develop a stable glassy system containing Fe and V_2O_5. Secondly, to develop some new glassy systems by expanding the former-modifier matrices via gradual doping of TeO_2, CuO etc. Thirdly, to examine the impact of mixed 'former-modifier' on their electrical and dielectric properties. Lastly, to get an insight into the composition-dependent microstructure and electrical transport phenomena of present glassy systems with different former-modifier ratios not only from an application point of view but also from academic interest.

II. EXPERIMENTAL PROCEDURE

Transition metal oxide doped glassy systems, $0.2Fe - 0.8(0.5\ V_2\ O_5 - 0.4\ CdO - 0.1\ ZnO)$ say sample-A, $0.2Fe - 0.8(0.5\ V_2\ O_5 - 0.4\ CdO - 0.05\ ZnO - 0.05\ TeO_2\ )$ say sample-B, $0.2Fe - 0.8(0.5\ V_2\ O_5 - 0.4\ CdO - 0.05\ ZnO - 0.05\ CuO)$ say sample-C and $0.2Fe - 0.8(0.5\ V_2\ O_5 - 0.4\ CdO - 0.05\ ZnO - 0.025\ TeO_2 - 0.025\ CuO\ )$ say sample-D, partially substitution of ZnO by TeO_2, CuO and the combination of TeO_2 and CuO were developed using solid state reaction route. Silver paste was painted on both sides of the as-developed samples to act as electrodes for conducting electrical and dielectric examinations. HIOKI (model no. 3532-50, Japan) made LCR meter was employed to perform electrical measurement at numerous temperatures in the wide frequency range: 42 Hz to 5 MHz. Powder X-ray diffraction (PXRD) study of all as-developed samples was executed using a Rich-Seifert XRD 3000P diffractometer.

III. RESULTS AND DISCUSSIONS

A. Powder-XRD (PXRD) Analysis

In the Powder X-ray diffraction (PXRD) analysis of as-prepared samples, different peaks has been identified, which are indicating the presence of several nanocrystallite phases such as, $Zn_3V_2O_8$ [JCPDS – 96-034-0378], Te_2O_5 [ICDD – 00-021-1205], $V_4Te_4O_{18}$ [JCPDS – 96-153-2829], $Cu_{1.9}O_{29}V_{12}$ [JCPDS – 96-202-0267], $FeO_{10.88}V_3Zn_2$ [JCPDS – 96-153-3624], $Cu_2O_7V_2$ [JCPDS – 96-900-7586], CdO_6V_2 [JCPDS – 96-152-7175], $Cd_{9.5}Zn_{0.5}$ [JCPDS – 96-], ZnO [JCPDS – 96-036-1451], CdO [JCPDS – 00-005-0640], ZnV [JCPDS – 00-050-0570], $Fe_{6.5035}V_{11.5}$ [JCPDS - 96-100-8122], $Cd_2O_7Te_2$ [JCPDS – 96-153-6334] and V_3O_5 [JCPDS – 96-153-0102] that have been identified from the spectra and correctly

indexed. To compute various parameters regarding their crystallite size, the conventional Scherrer relation was utilised. In this regard, the following relation may be projected [17]:

$$D' = \frac{0.89\lambda}{\beta_D \cos\theta} \tag{1}$$

Here, β_D is the full width at half maxima (FWHM or peak broadening), λ is the wavelength of X-ray source (0.154 nm,), and θ refers to the position of the peak in radians. Average crystallite size (D') has been estimated using Eq. (a) and they are presented in Table I with composition (x). It is found in Table I that D' decreases gradually up to sample C and shows a minimum. At sample D, it shows an increment. In this regard, the chemical disorder of supercooled glassy matrices with respect to the gradual substitution of ZnO by other oxides may play vital roles [17]. As we move from sample A to sample B, the disordering increases due to lowering of the free energy of the amorphous phase with respect to the crystalline phase [14, 17]. As the melting point of CuO is much higher than that of TeO_2, the average crystallite size in Sample-C is much lower than that in sample B [15–17]. But in sample D, the combination of CuO and TeO_2 may reduce the melting point of the mixture [13, 14, 17]. The formation of glassy matrices is expected to be associated with crystallographic irregularities or defects in terms of dislocation [17], which may play significant role in the electrical conduction process via polaron hopping. The dislocation density or defects per unit volume (δ) [17] may be presented as:

$$\delta = \frac{1}{D'^2} \tag{2}$$

The variation of dislocation density (δ) values with respect to composition is presented in Table I. It is clear from the results that δ increases initially with partial substitution of the former up to sample-C and a subsequent drop is observed after that. This variation in δ may indicate a transition from an unstable to a stabilized structure, resulting in reduced grain boundary impact [17]. The structural stability should be linked to their electrical transport properties, which will be discussed later.

Composition	Crystallite Size D′ (nm) (± 0.001)	Dislocation Density (δ) (± 0.0003)
A	20.7317	0.00233
B	19.3699	0.00267
C	18.2992	0.00299
D	21.6225	0.00214

TABLE I. The average values of crystallite size (D) and the dislocation density (δ) for the systems A, B, C and D respectively. Estimated errors are also included.

B. Scanning Electron Microscopic (SEM) Study

Fig. 1(a) and (b) show the scanning electron microscopic (SEM) images of examined systems, B and D respectively. The image in Fig. 1(a) shows ditellurium pentoxide (Te_2O_5) distributed ladder-type nanostructures [13–15, 17], which have already been confirmed from XRD study. Te_2O_5 should have the property to crystallize within the monoclinic $P2_1$ space group [17]. Owing to the presence of semiconducting tellurium in system B, it may be used as a good sensor, which may exhibit optical second order non-linearity [17]. In Fig. 1(b), the features of wrinkled morphology have been observed and these are due to the existence

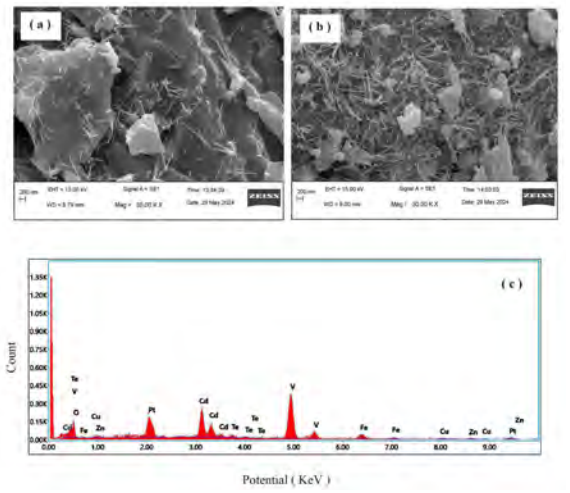

FIG. 1. SEM micrographs of (a) Sample B, (b) Sample D and EDAX of (c) Sample D, respectively.

of $Cu_{1.9}O_{29}V_{12}$ nanophases as confirmed by the XRD studies. Similarly, wide band gap semiconducting phases, $Cd_2O_7Te_2$ are also present as per phase-identification by XRD studies. So, mixed phases comprising $Cu_{1.9}O_{29}V_{12}$ and $Cd_2O_7Te_2$ in system D may allow it to absorb high-energy light of UV spectra [17]. Energy dispersive X-ray analysis (EDAX) has also been performed to analyse the identification of the elemental composition of the as-developed samples and EDAX image for sample-D is presented in Fig. 1(c). Using EDAX, the information about the chemical composition of as-developed samples including the presence of elements in the resultant composites are displayed in the inset of Fig. 1(c), which confirms the purity of the as-developed samples using this melt-quenching route [15, 17, 18] in the air environment.

C. AC Conductivity Study

The electric field influenced the synchronized migration of loosely bounded charge carriers, which in turn governs the thermally activated electrical conductivity in materials [17]. The frequency dependent electrical conductivity is one of the remarkable virtue of the materials that describes the behaviour and

dependency of dominating charge particles (such as holes/electrons or cations/anions) on the conduction mechanism and their response to changes in temperature [17]. The electrical conductivity of composite matrices can be expressed as [17]:

$$\sigma = \left(\frac{\nu_0 R^2 N e^2 k_B T}{1}\right) c(1-c) \exp(-2\alpha R) \exp\left(\frac{-E}{k_B T}\right) \tag{3}$$

and hence

$$\log\left(\frac{1}{\sigma T}\right) = \log\left(\frac{k_B}{\nu_0 R^2 N e^2 c(1-c)}\right) + \frac{2\alpha R}{2.303} + \frac{E_\sigma}{2.303 k_B T}. \tag{4}$$

Here, ν_0, e, N, R, c, and α represent the the optical phonon frequency, the electronic charge, the number of transition metal ion (TMI) sites per unit volume, the average distance between two TMIs, the redox ratio, and the decay component of the radial wave function respectively. The activation energy, denoted as E can be expressed as the combination of $E_p/2$ and $E_d/2$. Here, E_p and E_d represent the polaron-formation energy and the disorder energy respectively. This formulation represents the potential energy difference between two terminal sites.

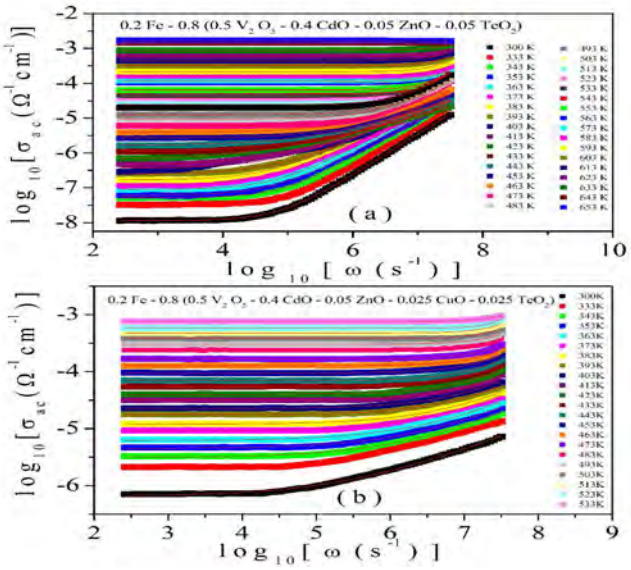

FIG. 2. The variation of temperature dependent AC Conductivity curves with frequency of (a) Sample B and (b) Sample D respectively.

D. Almond-West formalism

The AC conductivity spectra for sample-B and sample-D are presented in Fig. 2(a) and (b), respectively, at numerous temperatures, which may highlight the thermally activated nature of the present materials. Fig.

2 gives the impression that the conductivity of alternating current (AC). The lower frequency component of AC conductivity shows a frequency-independent regime, which may correspond to the conductivity of direct current (DC). The dispersion commences from the crossover region from DC to AC conductivity as shown in Fig. 2. This particular frequency is nomenclature as the cross-over frequency or the hopping frequency [17]. Additionally, it has been noted that the AC conductivity plots for different values of x are of a similar character. A significant amount of research has been conducted using the Almond-West formalism [17] to investigate frequency-dependent conductivity [17, 18]. As per Almond-West formalism [17, 18] the expression of AC conductivity takes the form:

$$\sigma(\omega) = \sigma_{dc}\left(1 + \frac{\omega^n}{\omega_H^n}\right). \tag{5}$$

Here, ω_H is referred to as the crossover of hopping frequency of charge carriers, n refers to the exponent of power low and σ_{dc} stands for the low frequency conductivity. AC conductivity data of as-developed system are well fitted using Almond-West Formalism [17, 18].

Experimental data are fitted well in Fig. 2(a) and (b) using Eq. (5), which helps to compute the values of ω_H, n and σ_{dc}. In Fig. 3(a), the variation of ω_H with temperature for the gradual substitution of ZnO by other oxides has been presented, which also exhibited thermally excited nature. Here, the nature of variation of ω_H is same as DC conductivity. The variation of n with respect to partially substitution of ZnO is depicted in Fig. 3(b). Higher values of n may be linked with the percolation [17–19] of charge carriers.

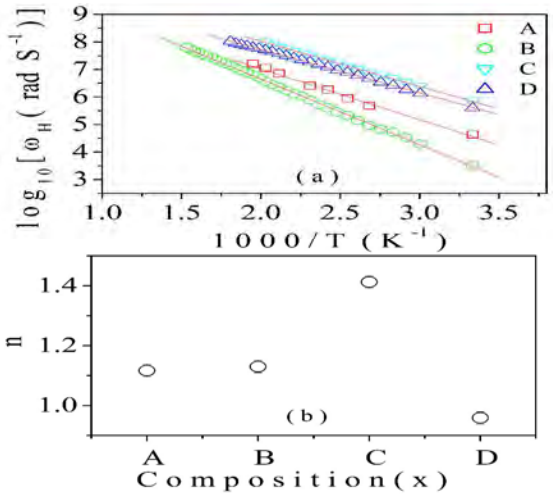

FIG. 3. The variation of temperature dependent AC Conductivity curves with frequency of (a) Sample B and (b) Sample D respectively.

E. Conductivity Spectra and Power Law Behavior

Fig. 4(a) illustrates the AC conductivity spectra of all as-developed samples at 413 K. Here, AC conductivity is found to change with the gradual substitution of ZnO by other oxides. To explore the nature of frequency dependent AC conductivity of amorphous semiconductors, Jonscher's power law [17–20] can be utilized. It takes the following form [17–20]:

$$\sigma(\omega) = \sigma_0 + A\omega^s, \tag{6}$$

where $\sigma(\omega)$ represents the total conductivity, while σ_0 refers to the conductivity at low frequencies, or direct current conductivity. This low-frequency conductivity exhibits a thermally excited nature. The pre-factor, "A" may be associated with the strength of the polarizability and s is the frequency power exponent. It represents the purely dispersive component of AC conductivity and follows a power law behaviour. The exponent s ranges from 0 to 1, indicating the extent and nature of interaction between the hopping of charge carriers and the surrounding lattices.

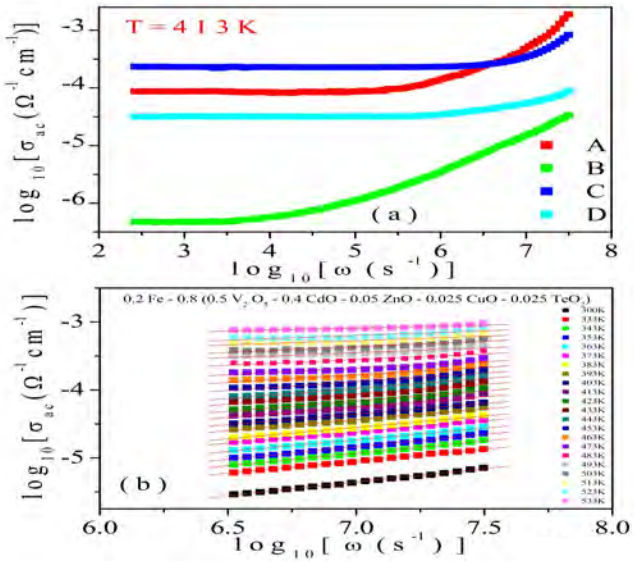

FIG. 4. Conductivity Spectra at 413 K of all as-developed samples; (b) Conductivity Spectra at high frequency at various temperatures for a particular sample-D.

The AC conductivity of the present system ex can exhibits transition from low frequency plateau to a dispersed high frequency region beyond a critical frequency (ω_c). In general, Jonscher's universal law [20] may provide a description of the AC conductivity component that highlights to the dispersive region. Ion-conducting glassy systems, polymers and disordered semiconductors, conducting polymer ceramics, strongly doped ionic crystals, and other materials have all shown this kind of behaviour [17–20]. A review of the literature found no evidence that the atomic units used to make up this reaction affected its

qualitative features [20]. Papathanassiou and his group [21] have concentrated on modeling the flow of electric charge carriers in an electric field within a framework of suitable conduction paths. The lengths of these conduction paths can be determined by analyzing the energy distributions within the potential energy profiles. For instance, in polymer networks, the conduction paths vary in length due to the distribution of polymer chain lengths, mechanical bond among various chains, cross-linking, and other factors [21]. In the present network structure, the available defects and lack of periodicity may be the possible reasons for the existence of conduction paths with variable lengths [19–21]. At lower frequencies, specifically below the critical frequency (ω_c), AC conductivity is almost a constant [18–20]. This phenomenon is primarily due to macroscopic behavior of conductivity, which occurs along paths that integrate the opposite surfaces of the sample where the electrodes are connected. This conductivity is related to the diffusive motion of polarons [17–20]. In contrast, at higher frequencies $\omega > \omega_c$, there is a dispersion in AC conductivity [18–20]. In this frequency range, the total conductivity consists of both macroscopic conductivity and conduction paths with variable lengths [18]. As a consequence, the AC conductivity depends on correlated and sub-diffusive movement of charge carriers (polarons) [17]. Fig. 4(b) displays the conductivity spectra in the high-frequency region at numerous temperatures, ranging from 300 K to 533 K, for system D. Fig. 4(b) clearly shows that the AC conductivity increases with temperature, indicating that it is thermally triggered. To find the values of s, the experimental data in Fig. 4(b) were fitted using Jonscher's power law model, as referenced in sources [17–20]. The solid lines in the figure represent these best-fit lines, and the slopes of these lines can be used to estimate the values of s. Multiple research studies have successfully applied several conduction models, such as correlated barrier hopping (CBH), quantum mechanical tunneling (QMT) model, hopping over a barrier (HOB), non-overlapping small polaron tunneling (NSPT) model and many more [17, 20]. Fig. 5 (a), (b), (c) and (d) show the s versus temperature (T) plots for as-developed samples A, B, C and D respectively. Figure 5 remarkably shows that the values of s decrease as the temperature increases for the gradual substitution of ZnO by other oxides. The relationship between s and temperature can be predicted from the dataset shown in Fig. 5. Several research studies [18–20] have been conducted to explore the transport phenomena of this system, yet comprehensive descriptions are still lacking. The temperature dependence of conductivity can be understood using a modified version of the correlated barrier hopping model (CBH) [19], which is believed to be the primary conduction mechanism. According to the CBH Model, the frequency exponent s can be expressed as [19]

$$S = 1 - \frac{6k_BT}{W_m + k_BT \cdot \ln(\omega\tau_0)}. \tag{7}$$

Here, k_B, T, W_m and τ_0 refer to the Boltzmann Constant, absolute temperature, maximum barrier height and the relaxation time respectively [17, 19]. To obtain well-fitted plots, the expression of the CBH model

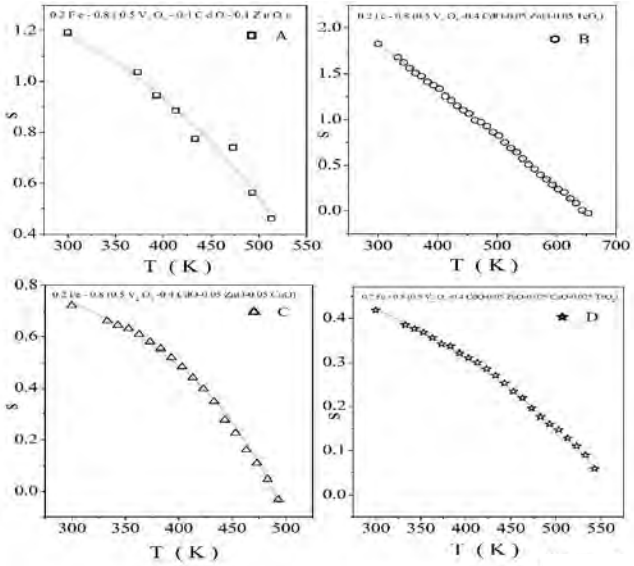

FIG. 5. S versus T plots of the A, B, C and D respectively. Solid lines refer to the best fitting using CBH Model (modified).

has been modified slightly and is presented below:

$$S = 1 - \frac{6k_B\,(T - T_0)}{W_m + k_B\,(T - T_0)\ln(\omega\tau_0)}. \tag{8}$$

As per CBH model [19], the expression of AC conductivity may take the form:

$$\sigma_{ac} = \frac{1}{24} n' \pi^3 N(E_F)^2 \varepsilon\varepsilon_0 \omega R_{H\omega}^6. \tag{9}$$

Here, $N(E_F)$ refers to the concentration of pair states, R_H represents the hopping distance at frequency ω and n' stands for the number of charge carriers (polarons) involved in the hopping conduction.

Sample	Activation Energy for Hopping Frequency (rad s^{-1}) ($\pm$0.01)	W_m (eV) ($\pm$0.10)	τ_0 (s) ($\pm$0.001)	T_0 (K) ($\pm$0.50)
A	0.36519	0.18228	2.24×10^{-6}	378.2294
B	0.47161	0.14805	3.37×10^{-13}	465.5276
C	0.32519	0.09739	9.37×10^{-13}	485.0123
D	0.31358	0.08149	8.69×10^{-18}	460.1194

TABLE II. Fitting parameters obtained from s versus T plots using CBH (Modified) model.

Table II presents the values of W_m, τ_0, and T_0, which were obtained from the optimal fitting of the S versus temperature plot illustrated in Fig. 5 using Eq. (8). The information in Table II indicates that the barrier height (W_m) reduces as the amount of ZnO is gradually replaced by other oxides (from sample A to sample D).

The CBH model indicates that the condition, $W_m \approx E_H$ (where E_H represents the activation energy associated with the hopping frequency) is necessary for the bi-polaron hopping mechanism as the major conduction process [17, 19]. However, when $W_m \approx 0.25E_H$, the conduction arises from the single polaron hopping process. The current study confirms that the condition, $W_m \approx 0.25E_H$ is satisfied, indicating that the hopping due to single polaron is the main mechanism. This finding is corroborated by a close and meaningful relationship between various parameters, attributed to the higher s values in the low-temperature zone.

IV. CONCLUSION

PXRD and SEM studies reveal various nanophases such as $Zn_3V_2O_8$ nanostructures in system A, Te_2O_5 distributed ladder-type nanostructures in system B, $Cu_2O_7V_2$ nanostructures with a distinctive wrinkled morphology in system C and $Cu_{1.9O29}V_{12}$ and $Cd_2O_7Te_2$ in system D. The estimated values of dislocation density (δ) are found to increase initially with partial substitution of former up to system C and a subsequent drop is observed after that. This nature of variation of δ may be an indication of a shift from an unstable to a stabilized structure with reduced grain boundary impact. Almond-West formalism and power law model have been employed to interpret AC conductivity dataset. Hopping of a single polaron is the primary process, displaying a strong relationship among various parameters of the current system.

ACKNOWLEDGMENTS

The financial assistance for the work by the Science and Engineering Research Board, Govt. of India via Sanction No: CRG/2023/000046 is thankfully acknowledged (PI: Dr. Sanjib Bhattacharya). Prof. Dipankar Chattopadhyay of University of Calcutta, West Bengal is gratefully acknowledged for providing SEM facility.

* ddirhrdc@nbu.ac.in

[1] N. F. Mott, Adv. Phys. **16** 49 (1967).

[2] D. Cao, X. Sun, Q. Li, A. Natan, P. Xiang, and H. Zhu, Matter **3**, 57 (2020).

[3] K. Kaup, J. D. Bazak, S. H. Vajargah, X. Wu, J. Kulisch, G. R. Goward, and L. F. Nazar, Adv. Energy Mater. **10**, 1902783 (2020).

[4] R. Zhao, G. Hu, S. Kmiec, J. Wheaton, V. M. Toress, and S. W. Martin, Batter. Supercaps. **5**, e202100356 (2022).

[5] S. Samanta, A. Maity, and D. Chakravorty, ACS Appl. Eng. Mater. **2**, 715 (2024).

[6] X. Lin, Y. Zhao, C. Wang, J. Luo, J. Fu, B. Xiao, Y. Gao, W. Li, S. Zhang, J. Xu, F. Yang, X. Hao, H. Duan, Y. Sun, J. Guo, Y. Huang, and X. Sun, Angew. Chemie Int. Ed. **63**, e202314181 (2024).

[7] U. Hoppe, A. Ghosh, S. Feller, A. C. Hannon, D. A. Keen, and J. Neuefeind, J. Non-Cryst. Solids **572**, 121120 (2021).

[8] R. V. Barde RV and S. A. Waghuley, J. Non-Cryst. Solids. **15**, 117 (2013).

[9] F. H. Margha, G. T. El-Bassyouni, and G. M. Turky, Ceram. Int. **45**, 11838 (2019).

[10] M. A. Algradee, A. B. Alwany, O. M. Samir, E. E. Saleh, and T. M. E. Sherbini, J. Non-Cryst. Solids **589**, 121664 (2022).

[11] S. Das and A. Ghosh, J. Non-Cryst. Solids **458**, 28 (2017).

[12] P. T. Rao, D. L. Sastry, and K. V. Ramesh, Phys. Chem. Glasses: Eur. J. Glass Sci. Technol. B **57**, 279 (2016).

[13] H. Satou and H. Sakata, Mater. Chem Phys. **14**, 186 (2000).

[14] T. Hasegawa., K. Takizawa and T. Walanbe, Kanagawa-Ken Kogyo Shikensho Kenkyo Hokoku **23**, 64 (1968).

[15] D. K. Jain and J. C. Garg, Indian J. pure appl. Phys. **17**, 642 (1979).

[16] J. P. Davim, Introduction to Mechanical Engineering, Springer International Publishing (2018).

[17] B. Karmakar, K. Rademann and A. Stepanov, “Glass Nanocomposites” Synthesis, Properties and applications, Elsevier (2016).

[18] A. Ghosh, J Chem Phys. **102**, 1385 (1995).

[19] N. F. Mott and E.A. Davis, Electronic Processes in Non-crystalline Materials, Clarendon, Oxford (1969).

[20] S. Ojha, M. Roy, A. Chamuah, K. Bhattacharya, and S. Bhattacharya, Phys. Chem. Chem. Phys. **22**, 24600 (2020).

[21] A. N. Papathanassiou, I. Sakellis, and J. Grammatikakis, Appl. Phys. Lett. **91**, 122911 (2007).